11th World Congress on Computational Mechanics (WCCM XI)
5th European Conference on Computational Mechanics (ECCM V)
6th European Conference on Computational Fluid Dynamics (ECFD VI)
E. Oñate, J. Oliver and A. Huerta (Eds)

IMPLEMENTATION AND VALIDATION OF HIGH-ACCURACY AEROACOUSTIC SCHEMES FOR THE DESCRIPTION OF VISCOUS GASFLOWS

ANATOL V. ALEXANDROV* AND LUDWIG W. DORODNICYN†

* M.V. Keldysh Institute for Applied Mathematics
Miusskaia sq. 4, 125047 Moscow, Russia
e-mail: alexandrov@imamod.ru

† M.V. Lomonosov Moscow State University, Faculty CMC
Vorobievy gory, 119991 Moscow, Russia
e-mail: dorodn@cs.msu.su

Key words: Dispersion-Relation-Preserving Schemes, Spectral Resolution, Navier-Stokes Equations, Numerical Boundary Conditions

Abstract. The work is devoted to further development of Dispersion-Relation-Preserving (DRP) scheme by C. Tam and coworkers as well as schemes by C. Bogey and C. Bailly aimed at their implementation to nonlinear viscous flows, so far as viscosity plays an important role in sound generation. We will carry out accuracy and stability testing of the numerical algorithms and present some advances in discrete boundary conditions. We concentrate at essentially viscous flows including the 2D Lamb–Oseen and the 3D Taylor–Green vortex decay as well as channel flows.

1 INTRODUCTION

In the field of computational aeroacoustics, the so-called Dispersion-Relation-Preserving (DRP) scheme by C. Tam and coauthors [1] is widely used. An analogous family of schemes by C. Bogey and C. Bailly [2] may be treated as an extension of the original DRP scheme.

The algorithms considered are based on high order of approximation coupled with the optimization of spectral resolution. Very small artificial dispersion and dissipation makes this class of schemes a reliable tool for the numerical integration of the linearized Euler equations as well as other hyperbolic systems of equations. However, for the simulation of viscous flows the technique of DRP schemes has been developed not so successfully [3].

Following [4], we represent the nonlinear Navier–Stokes equations in the 2D Cartesian coordinates as

$$\frac{\partial \mathbf{Q}}{\partial t} + \frac{\partial \mathbf{F}}{\partial x} + \frac{\partial \mathbf{G}}{\partial y} = \frac{\partial \mathbf{R}}{\partial x} + \frac{\partial \mathbf{S}}{\partial y}\,, \tag{1}$$

where $\mathbf{Q}$ is the vector of conservative variables, $\mathbf{F}$ and $\mathbf{G}$ are the convective fluxes, $\mathbf{R}$ and $\mathbf{S}$ are the viscous fluxes:

$$\mathbf{Q} = \begin{pmatrix} \rho & \rho u & \rho v & E \end{pmatrix}^T,$$
$$\mathbf{F} = \begin{pmatrix} \rho u & \rho u^2 + p & \rho uv & (E+p)\,u \end{pmatrix}^T, \qquad \mathbf{G} = \begin{pmatrix} \rho v & \rho uv & \rho v^2 + p & (E+p)\,v \end{pmatrix}^T,$$
$$\mathbf{R} = \begin{pmatrix} 0 & \tau_{xx} & \tau_{xy} & u\tau_{xx} + v\tau_{xy} - q_x \end{pmatrix}^T, \qquad \mathbf{S} = \begin{pmatrix} 0 & \tau_{xy} & \tau_{yy} & u\tau_{xy} + v\tau_{yy} - q_y \end{pmatrix}^T.$$

The vectors $\mathbf{R}$ and $\mathbf{S}$ contain the components of viscous stress tensor and heat flux

$$\tau_{xx} = \frac{4}{3}\,\mu\,\frac{\partial u}{\partial x} - \frac{2}{3}\,\mu\,\frac{\partial v}{\partial y}\,, \quad \tau_{xy} = \mu\,\frac{\partial v}{\partial x} + \mu\,\frac{\partial u}{\partial y}\,, \quad \tau_{yy} = -\frac{2}{3}\,\mu\,\frac{\partial u}{\partial x} + \frac{4}{3}\,\mu\,\frac{\partial v}{\partial y}\,,$$
$$q_x = -\lambda\frac{\partial T}{\partial x}\,, \quad q_y = -\lambda\frac{\partial T}{\partial y}\,. \tag{2}$$

This form of the Navier–Stokes equations is suitable for the discretization in terms of the DRP approach and for the formulation of numerical boundary conditions.

We carry out qualitative and quantitative assessment of the high-accuracy schemes on the known flows of viscous fluid at low Mach numbers and moderate Reynolds numbers. This includes the Lamb–Oseen vortex, the 3D Taylor–Green vortex, and the Poiseuille flow. Such benchmarks can demonstrate expected behavior of the algorithms in their future turbulent jet applications.

2 WIDE-STENCIL FINITE-DIFFERENCE SCHEMES

In the computational aeroacoustics, there is widely used an approach associated with high-accuracy schemes with spectral resolution frequently referred to as Dispersion-relation-preserving (DRP) schemes [1]. Such algorithms are based on uniform grids and involve wide stencils on which first spatial derivatives are approximated by centered differences as written below:

$$\left(\frac{\partial \varphi}{\partial x}\right)_j \sim \frac{1}{\Delta x}\sum_{l=-m}^{m} a_l \varphi_{j+l}\,. \tag{3}$$

Coefficients a_l are set according to a special procedure which includes the optimization of spectral resolution (see [1, 2]). We will consider the seven-point ($m = 3$) scheme from [1].

The numerical approximation to the Navier–Stokes equations relies on the application of an operator of type (3) for replacing all the spatial derivatives in both (1) and (2). This results in the following:

$$\frac{d\mathbf{Q}_{jk}}{dt} + \frac{1}{\Delta x}\sum_{l=-m}^{m} a_l \mathbf{F}_{j+l,k} + \frac{1}{\Delta y}\sum_{l=-m}^{m} a_l \mathbf{G}_{j,k+l} = \frac{1}{\Delta x}\sum_{l=-m}^{m} a_l \mathbf{R}_{j+l,k} + \frac{1}{\Delta y}\sum_{l=-m}^{m} a_l \mathbf{S}_{j,k+l}\,,$$
$$(\tau_{xx})_{jk} = \frac{4}{3}\,\mu\,\frac{1}{\Delta x}\sum_{l=-m}^{m} a_l u_{j+l,k} - \frac{2}{3}\,\mu\,\frac{1}{\Delta y}\sum_{l=-m}^{m} a_l v_{j,k+l}\,, \qquad \text{etc.} \tag{4}$$

For numerical time integration of (4) there exist a number of methods having high accuracy and optimized spectral resolution. We have chosen an explicit 5-stage Runge–Kutta scheme with low storage from [5].

3 BOUNDARY CONDITIONS

The stencil of finite difference (3) has half-width m. Consequently, such operators cannot be applied in m nodes near each of the boundaries. Eqs. (4) should be replaced by the same number of some other equations which we will treat as boundary conditions.

3.1 Artificial boundary conditions

The imposition of conditions at artificial boundaries is based on two backgrounds. First, it is a wide class of local nonreflecting boundary conditions for the Euler equations by [6]. Second, the consistent boundary conditions for large-stencil approximations to the advection equation by [7].

Consider the left boundary of the computational domain to be a subsonic inflow and the right boundary a subsonic outflow. As examples of continuous nonreflecting boundary conditions, we choose the inflow condition

$$\frac{\partial \mathbf{U}}{\partial t} - (c-u)\,\frac{\partial \mathbf{U}}{\partial x} = 0\,, \quad \mathbf{U} = (\,\rho\; u\; p\,)^T, \quad \frac{\partial v}{\partial t} = 0 \tag{5}$$

and the outflow condition

$$\begin{aligned} &\frac{\partial \rho}{\partial t} + u\,\frac{\partial \rho}{\partial x} + v\,\frac{\partial \rho}{\partial y} + \frac{1}{c}\,\frac{\partial p}{\partial x} = 0\,, \qquad \frac{\partial u}{\partial t} + (c+u)\,\frac{\partial u}{\partial x} + v\,\frac{\partial u}{\partial y} + c\,\frac{\partial v}{\partial y} = 0\,, \\ &\frac{\partial v}{\partial t} + u\,\frac{\partial v}{\partial x} + v\,\frac{\partial v}{\partial y} + \frac{1}{\rho}\,\frac{\partial p}{\partial y} = 0\,, \qquad \frac{\partial p}{\partial t} + (c+u)\,\frac{\partial p}{\partial x} + v\,\frac{\partial p}{\partial y} = 0\,. \end{aligned} \tag{6}$$

The discrete boundary conditions include approximations to nonreflecting conditions and expressions for the viscous fluxes (2). The both are implemented with the use of the biased differences by [7]. As an illustration of right-hand boundary conditions we show the discrete form of the last equation of (6) and the stress τ_{xx}:

$$\begin{aligned} &\left(\frac{\partial p}{\partial t}\right)_{N_x-j,k} + (c+u)_{N_x-j,k}\,\frac{1}{\Delta x}\sum_{l=0}^{2m} b_{jl}\,p_{N_x-l,k} + v_{N_x-j,k}\,\frac{1}{\Delta y}\sum_{l=-m}^{m} a_l\,p_{N_x-j,k+l} = 0\,, \\ &(\tau_{xx})_{N_x-j,k} = \frac{4}{3}\,\mu\,\frac{1}{\Delta x}\sum_{l=0}^{2m} b_{jl}\,u_{N_x-l,k} - \frac{2}{3}\,\mu\,\frac{1}{\Delta y}\sum_{l=-m}^{m} a_l\,v_{N_x-j,k+l}\,, \quad j = 0,\ldots,m-1. \end{aligned} \tag{7}$$

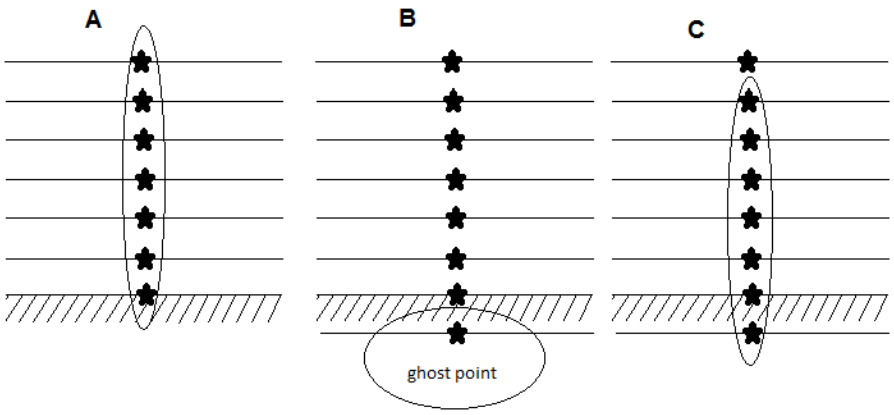

Figure 1: 7-point stencils of two types for approximation of y-fluxes

The left-hand boundary condition (5) and the expression for τ_{xx} become

$$\left(\frac{\partial \mathbf{U}}{\partial t}\right)_{jk} + (c-u)_{jk}\,\frac{1}{\Delta x}\sum_{l=0}^{2m} b_{jl}\mathbf{U}_{lk} = 0\,, \quad \mathbf{U} = (\,\rho\; u\; p\,)^T, \qquad \left(\frac{\partial v}{\partial t}\right)_{jk} = 0\,, \tag{8}$$

$$(\tau_{xx})_{jk} = -\frac{4}{3}\,\mu\,\frac{1}{\Delta x}\sum_{l=0}^{2m} b_{jl}u_{l,k} - \frac{2}{3}\,\mu\,\frac{1}{\Delta y}\sum_{l=-m}^{m} a_l v_{j,k+l}\,, \qquad j = 0,\ldots,m-1.$$

3.2 Solid wall conditions

Consider the boundary conditions on a solid surface which we assume to be a horizontal line $y = 0$ located below the fluid flow. The Navier–Stokes equations imply the no-slip conditions for the velocity components and an equation for temperature, e.g., the adiabatic condition:

$$u = v = 0\,, \quad \partial T/\partial y = 0\,. \tag{9}$$

Numerical solid wall conditions are based on the technique suggested in [4] and involving an additional row of 'ghost points' below the boundary nodes.

At near-boundary nodes, the governing Navier–Stokes equations (1)–(2) are approximated similarly to (4). For the y-derivatives there are used stencils of two types (see Fig. 1). The terms $\partial p/\partial y$ and $\partial \tau_{xy}/\partial y$ in (1) are treated on the stencil involving the ghost point and having the standard width $2m$, and the rest are, as usual, on the stencil within the physical domain.

Thus, the approximation to (1)–(2) has the form

$$\frac{d\mathbf{Q}_{jk}}{dt} + \frac{1}{\Delta x}\sum_{l=-m}^{m} a_l \mathbf{F}_{j+l,k} - \frac{1}{\Delta y}\sum_{l=0}^{2m} b_{kl}\mathbf{G}^{(1)}_{j,l} - \frac{1}{\Delta y}\sum_{l=-1}^{2m-1} b_{k+1,l+1}\mathbf{G}^{(2)}_{j,l}$$
$$= \frac{1}{\Delta x}\sum_{l=-m}^{m} a_l \mathbf{R}_{j+l,k} - \frac{1}{\Delta y}\sum_{l=0}^{2m} b_{kl}\mathbf{S}^{(1)}_{j,l} - \frac{1}{\Delta y}\sum_{l=-1}^{2m-1} b_{k+1,l+1}\mathbf{S}^{(2)}_{j,l}\,,$$
$$k = 0, \ldots, m-1, \qquad (10)$$
$$(\tau_{xx})_{jk} = \frac{4}{3}\,\mu\,\frac{1}{\Delta x}\sum_{l=-m}^{m} a_l u_{j+l,k} + \frac{2}{3}\,\mu\,\frac{1}{\Delta y}\sum_{l=0}^{2m} b_{kl} v_{j,l}\,, \qquad \text{etc.},$$

where fluxes $\mathbf{G}$ and $\mathbf{S}$ are divided onto two parts

$$\mathbf{G}^{(1)} = \begin{pmatrix} \rho v & \rho u v & \rho v^2 & (E{+}p)\, v \end{pmatrix}^T, \quad \mathbf{G}^{(2)} = \begin{pmatrix} 0 & 0 & p & 0 \end{pmatrix}^T,$$
$$\mathbf{S}^{(1)} = \begin{pmatrix} 0 & 0 & \tau_{yy} & u\tau_{xy} + v\tau_{yy} - q_y \end{pmatrix}^T, \quad \mathbf{S}^{(2)} = \begin{pmatrix} 0 & \tau_{xy} & 0 & 0 \end{pmatrix}^T,$$

and, for completeness, where the stencil is symmetric, we introduce the notation

$$b_{ml} = a_{m-l}\,,\ l = 0, \ldots, 2m.$$

At a ghost node ($k = -1$) values of pressure p and the shear stress τ_{xy} should be specified. Combining the Navier–Stokes equations (1) with the velocity conditions of (9) one obtains

$$\partial p/\partial x = \partial \tau_{xx}/\partial x + \partial \tau_{xy}/\partial y\,, \qquad (11)$$
$$\partial p/\partial y = \partial \tau_{xy}/\partial x + \partial \tau_{yy}/\partial y\,. \qquad (12)$$

Taking the discrete versions of Eqs. (11) and (12) for the wall node $k = 0$, we calculate the values of τ_{xy} and p, respectively, at the ghost point $k = -1$:

$$(\tau_{xy})_{j,-1} = -\frac{1}{b_{10}}\left[\frac{\Delta y}{\Delta x}\left(\sum_{l=-m}^{m} a_l p_{j+l,0} - \sum_{l=-m}^{m} a_l (\tau_{xx})_{j+l,0}\right) + \sum_{l=0}^{2m-1} b_{1,l+1}(\tau_{xy})_{j,l}\right], \qquad (13)$$
$$p_{j,-1} = \frac{1}{b_{10}}\left(-\frac{\Delta y}{\Delta x}\sum_{l=-m}^{m} a_l (\tau_{xy})_{j+l,0} + \sum_{l=0}^{2m} b_{0,l}(\tau_{yy})_{j,l} - \sum_{l=0}^{2m-1} b_{1,l+1} p_{j,l}\right). \qquad (14)$$

Second, we consider a modified boundary conditions which keep the mass conservation. They are based on the summation-by-parts (SBP) principle. The latter is particularly fulfilled when the mirror boundary conditions from [8] are used. To replace y-derivatives the standard stencils are implemented under the assumption of

$$\rho|_{-y} = \rho|_{y}\,, \quad v|_{-y} = -v|_{y}\,, \quad y \geq 0,$$

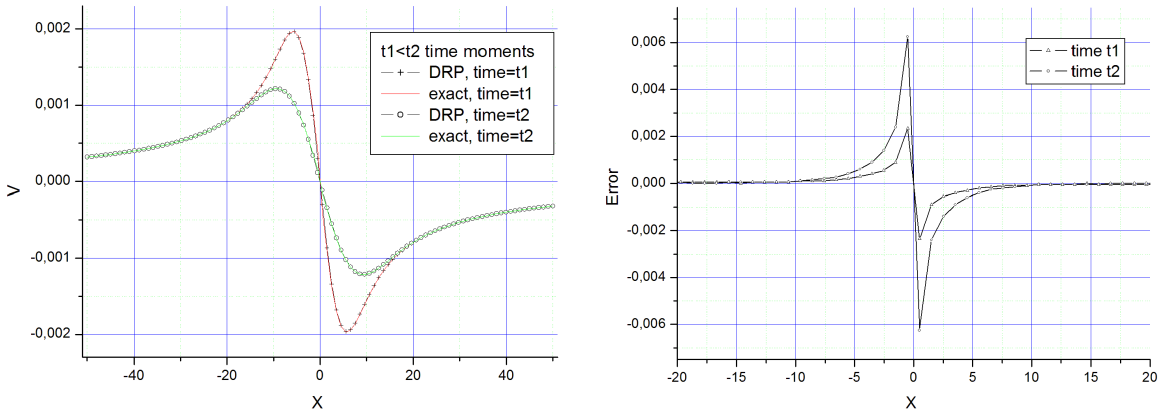

(a) (b)

Figure 2: (a) Velocity v versus x in section $y = 0$ for two time moments; (b) error $v - v_{ex}$

to be applied at ghost points. Such relations are exact in the case of linearized Euler equations and only approximate for the nonlinear Navier–Stokes.

We change the equation for density ρ in (10) as

$$\frac{d\rho_{jk}}{dt} + \frac{1}{\Delta x}\sum_{l=-m}^{m} a_l(\rho u)_{j+l,k} + \frac{1}{\Delta y}\left(\sum_{l=0}^{m+k} a_{l-k}(\rho v)_{jl} + \sum_{l=1}^{m-k} a_{l+k}(\rho v)_{jl}\right) = 0,$$
$$j = m, \ldots, N_x - m, \;\; k = 0, \ldots, m-1. \qquad (15)$$

For high-accuracy schemes, there exists a problem of interface between conditions on a solid surface and on an artificial boundary. We shall return to this question when considering a numerical example.

4 NUMERICAL RESULTS

4.1 Lamb–Oseen vortex

In the case of incompressible fluid, this problem has the analytical solution

$$u = -V(r,t)\, y/r, \quad v = V(r,t)\, x/r, \qquad (16)$$
$$V(r,t) = \frac{\Gamma}{2\pi r}\left(1 - \exp\{-\frac{r^2}{4\nu t}\}\right), \quad r = \sqrt{x^2 + y^2}.$$

This solution possesses a singularity at the origin point $r = 0$ as time t approaches zero, namely,

$$V(r,t) \approx \frac{\Gamma}{8\pi}\,\frac{r}{\nu t}\,, \;\; r \to 0. \qquad (17)$$

The computational domain is square $\{-L < x < L\} \times \{-L < y < L\}$. We used a uniform rectangular grid of $N_x \times N_y = 100 \times 100$, with mesh size $\Delta x = \Delta y = 1$.

As the artificial boundary conditions at the four sides of the square the Dirichlet-type conditions were specified. This means, for a discrete problem, the constant values of all the gas-dynamic parameters taken from infinity and imposed at the near-boundary nodes:

$$\rho \equiv \rho_{jk} = \rho_0, \quad u = v = 0, \quad p = p_0, \quad \tau_{xx} = \tau_{xy} = \tau_{yy} = q_x = q_y = 0,$$
$$j = 0, \ldots, m{-}1,\ N_x{-}m{+}1, \ldots, N_x \quad \text{or} \quad k = 0, \ldots, m{-}1,\ N_y{-}m{+}1, \ldots, N_y\,.$$

We choose the initial time to fulfill the requirement of bounded velocity throughout the numerical grid domain, i.e. $V(\Delta x, t_0) \approx Mc$ in (17), with M Mach number and c speed of sound. This leads to the value of

$$t_0 = \frac{\Gamma \Delta x}{8\pi M \nu c}\,.$$

For this time we calculate function $V(r, t_0)$ from (16) and specify the exact solution as an initial condition. We set $M = 0.1$ which means a weakly compressible flow. Constant values of pressure and density were set, $p = p_0$ and $\rho = \rho_0$.

Figure 2(a) shows the 1D distributions of transversal velocity v along the x-axis for two different time moments $t_1 < t_2$. In Fig. 2(b) the normalized error $(v - v_{ex})/v_*$ can be seen, where $v_{ex} = v_{ex}(x, y, t)$ is the exact solution from (16) and

$$v_* = 0.002 \approx \max v_{ex}(x, y, t_1).$$

The error is very small. A noticeable discrepancy between the numerical and exact solutions is located within the area of strong gradients and, consequently, large wavenumbers.

4.2 2D Taylor–Green vortex

The initial Taylor–Green vortex is set up by the formulas

$$u = U \sin(x/L)\cos(y/L), \quad v = -U\cos(x/L)\sin(y/L),$$
$$p = p_0 + (\rho_0 U^2/8)\,[\cos(2x/L) + \cos(2y/L)]\,.$$

Temperature $T = T_0$, density $\rho = p/(RT)$. The computational domain is cube $-\pi L < x, y < \pi L = 50$ supplied with periodic boundary conditions in both x and y.

The Mach number $M \equiv U/c_0 = 0.1$, so the flow is weakly compressible. The Reynolds number is defined by

$$\mathrm{Re} = \rho_0 U L/\mu_0\,. \tag{18}$$

We demonstrate the results for moderate Reynolds number $\mathrm{Re} = 100$.

We use a uniform rectangular grid of $N_x \times N_y = 100 \times 100$, with mesh size $\Delta x = \Delta y = 1$.

The 2D problem for the incompressible fluid has the exact solution which consists of exponential decay of initial vortex with unchanged shape:

$$u_{ex} = u(x, y, 0)\exp\{-2\nu t/L^2\}, \quad v_{ex} = v(x, y, 0)\exp\{-2\nu t/L^2\},$$
$$p_{ex} = p_0 + (\rho_0 U^2/8)\,[\cos(2x/L) + \cos(2y/L)]\exp\{-4\nu t/L^2\}.$$

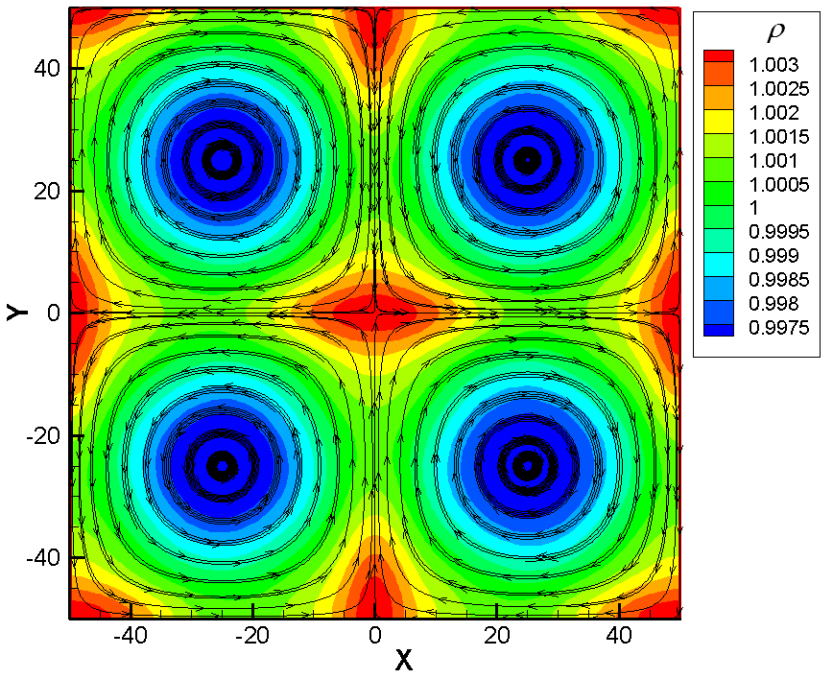

Figure 3: 2D Taylor–Green vortex; streamlines and distribution of density ρ

In the numerical experiment we see some anisotropy of the flow. Figure 3 displays essentially non-circular levels of density ρ in a number of areas. The comparison with the exact solution is shown in Fig. 4. The normalized error $(u - u_{ex})/U$, as seen in Fig. 4(b), is rather small and diminishes as time t grows. The latter can be explained by the dissipation process which concerns the error too. Note that the scale of the error is much bigger than in the previous case of Lamb–Oseen vortex. Possibly, this is due to the effect of compressibility and, second, the presence of flow anisotropy which causes an evident phase change between times t_1 and t_2.

4.3 3D Taylor–Green vortex

For the 3D case, the initial Taylor–Green vortex has the form

$$u = U\sin(x/L)\cos(y/L)\cos(z/L), \quad v = -U\cos(x/L)\sin(y/L)\cos(z/L), \quad w = 0,$$
$$p = p_0 + (\rho_0 U^2/16)\left[\cos(2x/L) + \cos(2y/L)\right](\cos(2z/L) + 2)\,.$$

Temperature $T = T_0$, density $\rho = p/(RT)$. The computational domain is cube $-\pi L < x, y, z < \pi L = 32$ supplied with periodic boundary conditions at each of the 6 faces.

The Reynolds number from (18) equals $\mathrm{Re} = 100$. This corresponds to the laminar regime of vortex decay [9].

We use a uniform rectangular grid of $N_x \times N_y \times N_z = 64^3$ nodes, with mesh size $\Delta x = \Delta y = \Delta z = 1$.

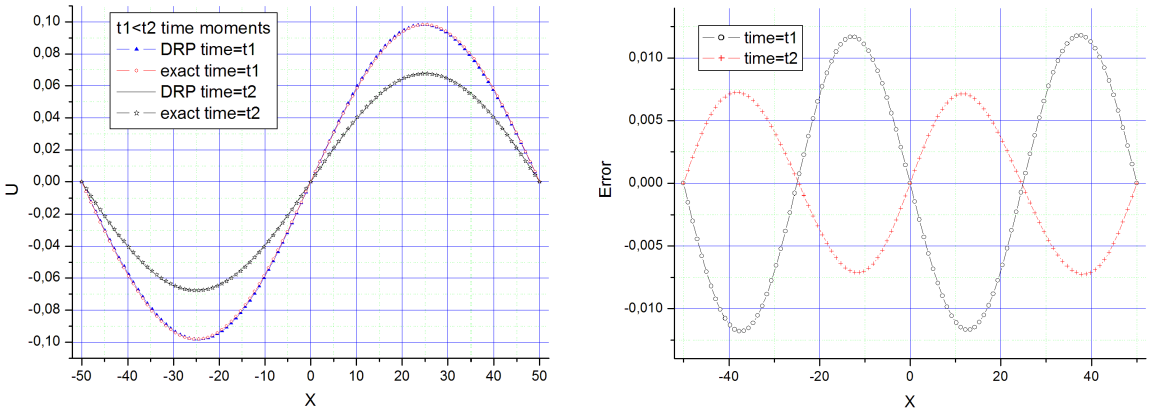

(a) (b)

Figure 4: (a) Velocity u versus x in section $y = 0$ for two time moments; (b) error $u - u_{ex}$

The subject for consideration (see, e.g., [10]) is the velocity curl $\vec{\omega} = \mathrm{rot}\,\vec{u}$, especially its z-component $\omega_z = \partial v/\partial x - \partial u/\partial y$. Figure 5 shows the isosurfaces of ω_z for initial time $t = 0$ and an intermediate time $t = 5$, when the flow loses isotropy though remains symmetric.

An example of flow pattern in the central 2D section $z = 0$ is shown in Fig. 6. The streamlines display an essentially three-dimensional nature of the flow, since there exist both positive and negative sources. Velocity in z-direction is significantly non-zero and comparable to the maximal amplitude $U = 0.1$.

The problem has no exact solution. The main quantitative characteristic of the flow [9] is the time evolution of the mean kinetic energy

$$E_k(t) = \frac{1}{8\pi^3 L^3 \rho_0 U^2} \int\limits_{\Omega} (1/2)\,\rho(u^2 + v^2 + w^2)\,dxdydz$$

In Fig. 7 its value is plotted with respect to dimensionless time $t \mapsto t/t_0$, where $t_0 = L/U$. Besides, the energy dissipation rate $-dE_k/dt$ is shown. The numerical results exhibit good correspondence with the reference data [9].

4.4 Flow in infinite duct

Next consider the 2D flow of a viscous gas inside an infinite channel (a compressible version of the Poiseuille flow). Steady-state computations in terms of the Navier–Stokes equations (1) have been carried out. The flow domain $\{-\infty < x < \infty\} \times \{-h < y < h\}$, where lines $y = \pm h$ are solid walls, was cut in x-direction as $\{-X < x < X\}$ for computations (see Fig. 8). The 7-point DRP scheme (4) with $m = 3$ was used for numerical solution.

The initial condition corresponds to the steady Poiseuille flow of an incompressible

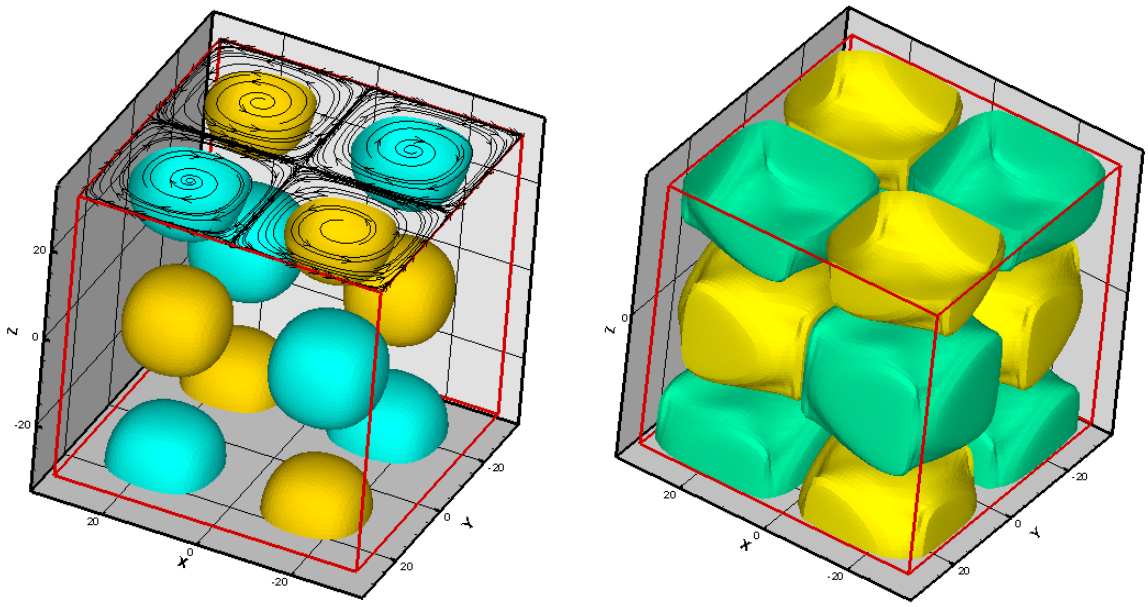

(a) (b)

Figure 5: Isosurfaces of the z-component of velocity curl ω_z for two values at (a) initial time and (b) $t = 5$

fluid:

$$\rho\big|_{t=0} \equiv \rho_0\,, \quad p\big|_{t=0} = p^{(0)}(x) \equiv p_0 + p_x x\,,$$
$$u\big|_{t=0} = u^{(0)}(y) \equiv u_{\max}\left[1 - (y/h)^2\right], \quad v\big|_{t=0} \equiv 0, \tag{19}$$

where ρ_0 and p_0 are reference values of density and pressure, $p_x < 0$ is a constant pressure gradient, and

$$u_{\max} = \frac{-p_x h^2}{2\mu_0} \tag{20}$$

is the maximum velocity given by theory.

At the left-hand boundary we set Eq. (5) modified allowing for the pressure gradient in the background Poiseuille flow (19):

$$\partial\rho/\partial t - (c-u)\,\partial\rho/\partial x = 0\,, \qquad \partial u/\partial t - (c-u)\,\partial u/\partial x = 0\,,$$
$$\partial p/\partial t - (c-u)\,\partial p/\partial x = -(c-u)\,p_x\,, \qquad \partial v/\partial t = 0\,. \tag{21}$$

On the right we used a shortened form of (6) with right-hand sides added:

$$\frac{\partial\rho}{\partial t} + u\,\frac{\partial\rho}{\partial x} + \frac{1}{c}\,\frac{\partial p}{\partial x} + v\,\frac{\partial\rho}{\partial y} = 0\,, \qquad \frac{\partial u}{\partial t} + (c+u)\,\frac{\partial u}{\partial x} + v\,\frac{\partial u}{\partial y} = 0\,,$$
$$\frac{\partial v}{\partial t} + u\,\frac{\partial v}{\partial x} + v\,\frac{\partial v}{\partial y} = 0\,, \qquad \frac{\partial p}{\partial t} + (c+u)\,\frac{\partial p}{\partial x} + v\,\frac{\partial p}{\partial y} = (c+u)\,p_x\,. \tag{22}$$

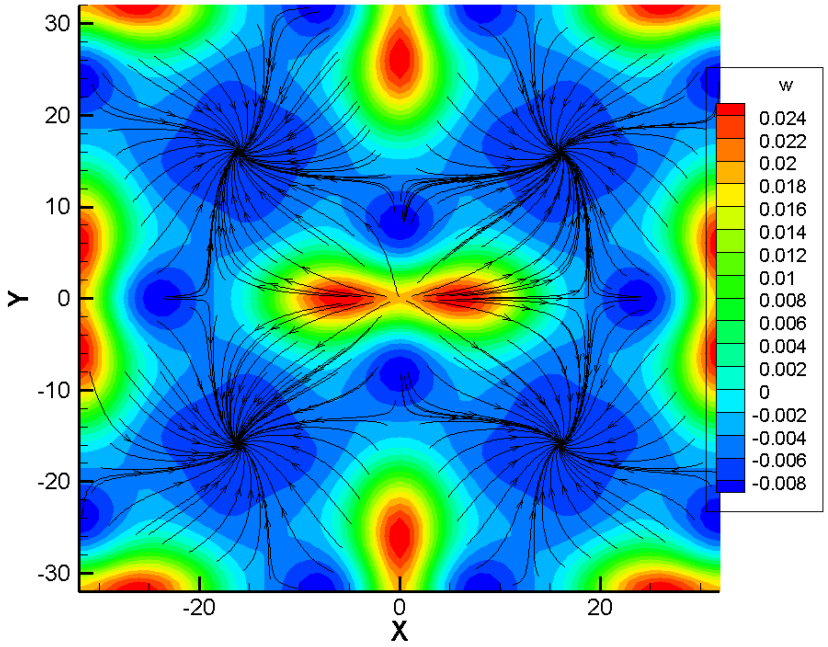

Figure 6: 3D Taylor–Green vortex; streamlines and distribution of z-velocity w

Discretization of Eq. (21), as well as of the viscous terms, was taken from (8). For Eq. (22) formulas (7) were used. At the bottom boundary the equation sets (10), (13)–(14) were imposed, whereas their mirror analogues were at the top boundary.

The equations at adjacent boundaries were coordinated with each other in order to obtain correct formulations in the corners (Fig. 8). In the upper left and lower left 3-by-3 corner zones, the artificial boundary condition (21), (8) was specified, with the change in representation of y-derivatives involving oblique stencils. In this case the no-slip condition (9) for velocities u and v at boundary points ($k = 0$) is fulfilled automatically, whereas the full version (6) contradicts the wall condition.

In the upper right and lower right corner zones, the boundary condition (22), (7) was specified with the use of oblique stencils for y-derivatives. The no-slip condition (9) is satisfied.

The Mach number is $M \equiv u_{\max}/c_0 = 0.1$ and the Reynolds number is $\mathrm{Re} \equiv 2u_{\max}\rho_0 h/\mu_0 = 20$. The domain size is $2X \times 2h = 400 \times 50$. A uniform rectangular grid of $N_x \times N_y = 400 \times 50$, with mesh size $\Delta x = \Delta y = 1$, was used in the computations.

The computations resulted in fast establishing a steady state characterized by almost parallel streamlines (Fig. 8 (a)) and nearly parabolic distribution of x-velocity u across the duct. Density ρ, being initially constant (19), acquires slightly nonuniform state (Fig. 8 (b)): $\min \rho = 0.9655$, $\max \rho = 1.0256$. The use of SBP condition (15) yields practically the same density distribution.

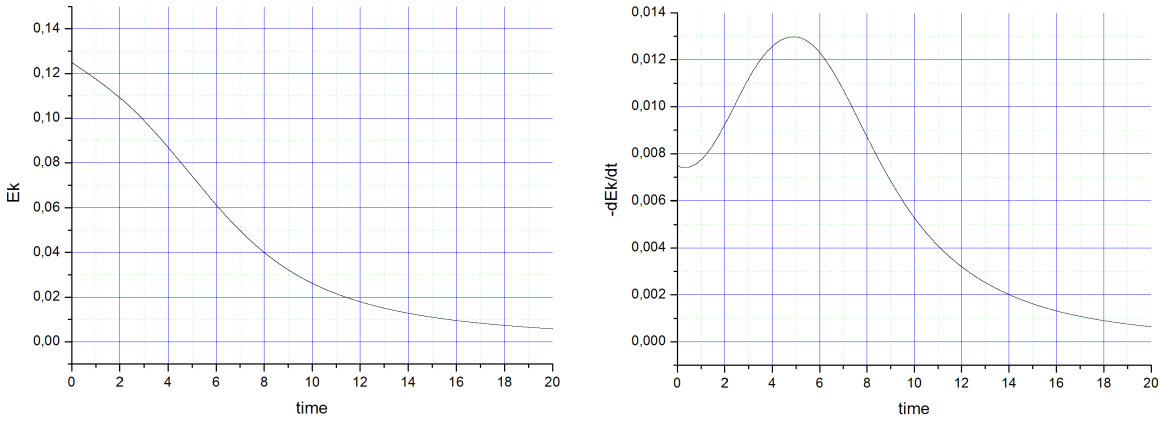

(a) (b)

Figure 7: Time evolution of the mean kinetic energy E_k (a) and its dissipation rate $-dE_k/dt$ (b)

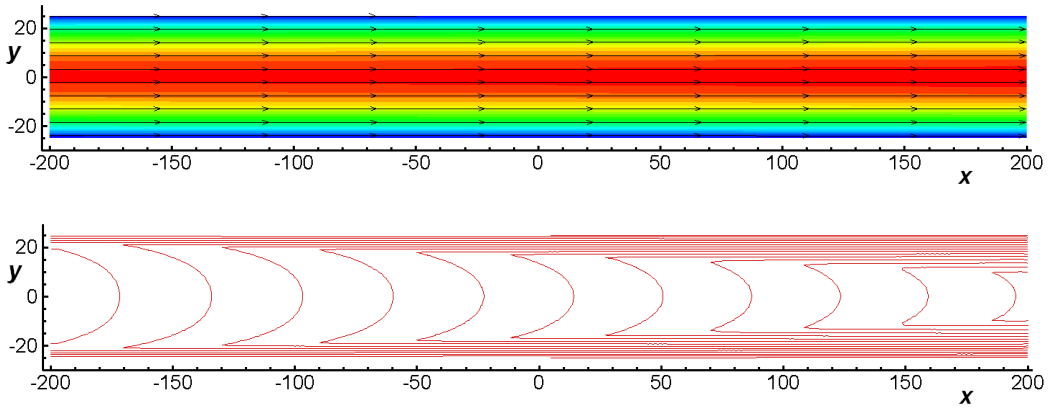

(a)

(b)

Figure 8: Flow in infinite duct; steady-state spatial distributions of x-velocity (a) and density (b)

REFERENCES

[1] Tam, C.K.W. and Webb, J.C. Dispersion-relation-preserving finite difference schemes for computational acoustics. *J. Comput. Phys.* (1993) **107**:262–281.

[2] Bogey, C. and Bailly, C. A family of low dispersive and low dissipative explicit schemes for flow and noise computations. *J. Comput. Phys.* (2004) **194**:194–214.

[3] Tam, C.K.W. Computational aeroacoustics: An overview of computational challenges and applications. *Int. J. Comput. Fluid Dynamics* (2004) **18**:547–567.

[4] Tam, C.K.W. and Dong, Zh. Wall boundary conditions for high-order finite-difference schemes in computational aeroacoustics. *Theor. Comput. Fluid Dynamics* (1994) **6**:303–322.

[5] Calvo, M., Franco, J.M., and Randez, L. A new minimum storage Runge-Kutta scheme for computational acoustics. *J. Comput. Phys.* (2004) **211**:1–12.

[6] Dorodnitsyn, L.V. Artificial boundary conditions for numerical simulation of subsonic gas flows. *Computational Mathematics and Mathematical Physics*, (2005) **45**:1209–1234.

[7] Dorodnicyn, L.W. Artificial boundary conditions for high-accuracy aeroacoustic algorithms. *SIAM J. Scientific Computing* (2010) **32**:1950–1979.

[8] Dorodnicyn, L.W. High-accuracy finite-difference boundary conditions for two-dimensional aeroacoustic problems. *Matematicheskoye Modelirovaniye* (2011) **23**:131–155. (In Russian)

[9] Brachet, M., Meiron, D., Orszag, S., et al. Small-scale structure of the Taylor-Green vortex. *J. Fluid Mech.* (1983) **130**:411–452.

[10] Elizarova, T.G. and Shirokov, I.A. *Laminar and turbulent regimes of the Taylor-Green vortex decay.* Keldysh Inst. Applied Math., Moscow, Russia, Preprint No.63, (2013). (In Russian)